

Article

Constructing a Quasi-Liquid Interphase to Enable Highly Stable Zn-Metal Anode

Junzhang Wang ¹, Zhou Xu ¹, Tengteng Qin ¹, Jintian Wang ¹, Rui Tian ¹, Xingzhong Guo ^{1,2,*}, Zongrong Wang ¹, Zhongkuan Luo ³ and Hui Yang ^{1,3}

¹ State Key Laboratory of Silicon and Advanced Semiconductor Materials, School of Materials Science and Engineering, Zhejiang University, Hangzhou 310058, China

² Hangzhou Global Scientific and Technological Innovation Center, Zhejiang University, Hangzhou 311200, China

³ Zhejiang-California International Nanosystems Institute, Zhejiang University, Hangzhou 310058, China

* Correspondence: msewj01@zju.edu.cn

Abstract: Rechargeable aqueous Zn-metal batteries have attracted widespread attention owing to their safety and low cost beyond Li-metal batteries. However, due to the lack of the solid electrolyte interphase, problems such as dendrites, side reactions and hydrogen generation severely restrict their commercial applications. Herein, a quasi-liquid interphase (QLI) with a “solid–liquid” property is constructed to stabilize the Zn-metal anode. The synergistic effect of solid and liquid behavior ensures the stable existence of QLI and simultaneously enables the interphase dynamic and self-adaptive to the anode evolution. Electrolyte erosion, Zn^{2+} diffusion and side reactions are inhibited during long-term cycling after introducing QLI, significantly improving the cycling stability and capacity retention of the symmetric and full cells modified with QLI ($Zn@QLI$), respectively. Constructing an interphase with a quasi-liquid state represents a promising strategy to stabilize the metal anodes in aqueous electrolytes and even extend to organic electrolytes.

Keywords: Zn-metal battery; quasi-liquid interphase; gelatin



Citation: Wang, J.; Xu, Z.; Qin, T.; Wang, J.; Tian, R.; Guo, X.; Wang, Z.; Luo, Z.; Yang, H. Constructing a Quasi-Liquid Interphase to Enable Highly Stable Zn-Metal Anode. *Batteries* **2023**, *9*, 328. <https://doi.org/10.3390/batteries9060328>

Academic Editor: Nam-Soon Choi

Received: 24 April 2023

Revised: 31 May 2023

Accepted: 9 June 2023

Published: 16 June 2023



Copyright: © 2023 by the authors. Licensee MDPI, Basel, Switzerland. This article is an open access article distributed under the terms and conditions of the Creative Commons Attribution (CC BY) license (<https://creativecommons.org/licenses/by/4.0/>).

1. Introduction

Since the commercialization of lithium-ion batteries (LIBs) in 1901, LIBs are widely applied in consumer electronics, electric vehicles and energy storage systems [1,2]. To pursue higher energy density, lithium batteries tend to adopt active lithium metal as the anode, combined with the flammable organic liquid electrolytes, causing lithium batteries inherently unsafe [3–6]. Zinc batteries with non-aqueous electrolytes fail to fundamentally solve the safety issues, and their performance is inferior to LIBs. In contrast, zinc metal batteries (ZMBs) based on neutral or weakly acidic aqueous electrolytes are intrinsically safe, coupled with low toxicity, high volumetric capacity (5855 mAh cm^{-3}) [7] and low cost, making them one of the most promising candidates in the grid-scale energy storage system [8–10]. However, similar to many metal anodes, the Zn-metal anode suffers from notorious dendrite growth as well as severe side reactions [11–13]. Moreover, zinc metal will inevitably be corroded by water and generate hydrogen due to its more negative reduction potential than hydrogen (-0.76 V vs. SHE) [14–16]. As a result, low Coulombic efficiency (CE), elevated polarization, short service life and even short circuit or structural damage seriously limit the commercialization of ZMBs [17–21].

To overcome these issues, great progress has been made around the Zn-metal anode, including intrinsic zinc engineering [22,23], interface modification [24–26] and electrolyte additives [27–29]. In contrast to LIBs, there is no solid–electrolyte interphase (SEI) formed on the surface of the Zn-metal anode [30,31]. Therefore, the surface coating strategy can effectively protect it from the above-mentioned problems by blocking direct contact of zinc with electrolyte. For example, Ma et al. recently constructed a highly electronically

insulating but highly Zn^{2+} -ion-conductive ZnF_2 layer on the Zn surface utilizing an *in situ* ion metathesis method, which prohibits over 99.2% parasitic hydrogen evolution and guides uniform Zn deposition [32]. Nonetheless, as many other approaches, few strategies follow the original nature of aqueous ZMBs, namely, low cost and environmentally friendly. In addition, many nano-materials without intrinsic Zn^{2+} ion conductivity have also been tried to build a modified layer on the zinc surface, including ZnO [33], TiO_2 [34], $CaCO_3$ [35], ZrO_2 [36] and MOFs [37]. However, such an interphase usually exhibits non-ideal Zn^{2+} ion conductivity and affinity with aqueous electrolytes, especially when organic binders are used to maintain its integrity.

More importantly, at the microscopic scale, a solid-state interphase cannot durably keep in close contact with the Zn-metal anode during the plating/stripping process, particularly when the applied pressure is small. Although a liquid interphase can completely match the electrode changes, it is difficult to prepare and exist stably between the electrode and liquid electrolyte. The gel electrolytes can also adapt to the surface changes, yet at the cost of sacrificing the excellent kinetic properties of the liquid electrolytes [38]. Inspired by the SEI of lithium batteries [39–41], the interphase between the Zn-metal anode and electrolyte should be electronically insulated, ionic conductive and compatible with the electrode and electrolyte, meanwhile, following the original nature of ZMBs. An interphase between solid and liquid states would provide new advances.

In this work, a quasi-liquid interphase (QLI) is constructed between the Zn-metal anode and aqueous electrolyte of ZMBs. Their solid characteristic ensures the stable existence of the interphase on the Zn-metal anode, while the liquid behavior enables the interphase dynamic and self-adaptive with the evolution of the zinc anode, ensuring a long-lasting conformal coating during aging or charge/discharge processes. As a consequence, the QLI-modified Zn-metal anode (denoted as $Zn@QLI$) exhibits highly stable cycling compared to the bare Zn anode. The QLI with green, scalability and cost-effectiveness can be directly transplanted to other metal anodes (e.g., Zn, Al, Mg and Ca) in aqueous batteries.

2. Materials and Methods

2.1. $Zn@QLI$ Synthesis

The QLI was prepared by a simple coating method followed by a sol–gel process. Firstly, gelatin powder (2 g, ~250 g Bloom, for microbiology, Aladdin) was immersed in 1.25 M $ZnSO_4$ (10 mL, AR, Sinopharm, Shanghai, China) aqueous solution at 25 °C for 30 min. After water swelling, the gelatin solution was dissolved at 60 °C and casted onto the polished Zn foils (~20 µm) with a scraper preheated to 60 °C. Then, the modified Zn foil was dried in the atmosphere at 25 °C overnight. The thickness of the modified layer is ~3 µm (Figure S1). $Zn@QLI$ was realized after immersing the modified Zn into the aqueous electrolyte, because gelatin molecules are able to swell and absorb 5~10 times their mass in water without losing the cross-linking structure, which gives it a “solid–liquid” characteristic [42].

To explore the swelling ability of $ZnSO_4$ electrolytes for gelatin, 1.5 M $ZnSO_4$ solution was also used to prepare gelatin solutions with the same procedure of 1.25 M $ZnSO_4$. The preparation processes of modified Cu foil ($Cu@QLI$) were the same as that of $Zn@QLI$, except that Zn foil was replaced by Cu foil (~20 µm).

2.2. $V_2O_5 \cdot 1.6H_2O$ Cathode Synthesis

$V_2O_5 \cdot 1.6H_2O$ was synthesized by the hydrothermal method according to a previous report [43]. V_2O_5 (0.35 g, AR, Sinopharm, Shanghai, China) and H_2O_2 (2 mL, 30%, Sinopharm, Shanghai, China) were dissolved in ultra-pure water (30 mL), then the solution was poured into a Teflon autoclave and heated at 200 °C for 6 h. Finally, the product was washed with water and freeze-dried.

2.3. Material Characterization

Scanning electron microscope (SEM) and energy-dispersive X-ray spectrometer (EDS) images were obtained on a Hitachi SU8010 (Tokyo, Japan) equipped with an Oxford Inca X-Max EDX (Oxford, UK). X-ray powder diffraction (XRD) was carried out on an Empyrean 200895 X-ray diffractometer (Shanghai, China) with Cu K α radiation. X-ray photoelectron spectroscopy (XPS) was conducted on a Thermo Scientific K-Alpha (Waltham, MA, USA) using an Al K α source.

2.4. Electrochemical Analysis

Cu-Zn and Cu@QLI-Zn half cells were assembled in CR2032-type coin cells at atmosphere containing 2 M ZnSO₄ (AR, Sinopharm, Shanghai, China) aqueous electrolyte (120 μ L) and a glass fiber separator (GF/A, Whatman, Maidstone, UK). To test the CEs, a fixed areal capacity (1.0 or 3.0 mAh cm $^{-2}$) was plated on the current collectors and then stripped away with a cutoff voltage of 0.5 V (vs. Zn/Zn $^{2+}$) at 0.2 or 1.0 mA cm $^{-2}$ in each cycle.

Unless specified otherwise, Zn-Zn and Zn@QLI-Zn@QLI symmetric cells were assembled in CR2032-type coin cells at atmosphere containing 2 M ZnSO₄ aqueous electrolyte (120 μ L) and a glass fiber separator. Some symmetric cells without separators were assembled in a homemade removable cell or an electrochemical reaction cell. Galvanostatic charge/discharge cycles were tested on a Land battery tester (CT3001A, 5 V/10 mA, Wuhan, China). Electrochemical impedance spectroscopy (EIS), Tafel polarization and chronoamperogram (CA) measurements were carried out on an electrochemical workstation (CHI 660E, Chenhua, Shanghai, China). EIS was made at an open circuit, and a frequency range of 100 kHz to 0.01 Hz was used with a perturbation amplitude of 5 mV. Tafel polarization and CA were conducted in a three-electrode configuration, where polished Zn or Zn@QLI was used as the working electrode, polished Zn as the counter and saturated calomel electrode as the reference.

Zn-V₂O₅ and Zn@QLI-V₂O₅ full cells were assembled in CR2032-type coin cells. An aqueous electrolyte containing 2 M ZnSO₄ (120 μ L) was used. The cathode was prepared by mixing V₂O₅, polyvinylidene fluoride (PVDF) and Ketjen black in a weight ratio of 7:2:1 with N-methyl-2-pyrrolidone (NMP) as solvent. The obtained slurry was cast onto a Ti foil and then dried at 80 °C for 8 h under vacuum. The loading of active materials is ~1.5 mg cm $^{-2}$. A ~20 μ m Zn foil is used as an anode, and the negative-to-positive ratio (N/P) is ~30. Galvanostatic charge/discharge cycles were tested on a Land battery tester between 0.2 and 1.6 V vs. Zn $^{2+}$ /Zn. Cyclic voltammetry (CV) tests were conducted on an electrochemical workstation in the voltage range of 0.2~1.6 V.

Electrode resistance tests were carried out by immersing Zn or Zn@QLI pieces in the electrolyte. All the anode pieces after electrochemical tests, including symmetric cell measurements, full cell measurements and resistance test, were frozen with liquid nitrogen and then freeze-dried for various characterizations. Unless specified otherwise, the freeze-dried QLI was peeled off from the Zn@QLI anode before analysis.

3. Results and Discussion

To construct a QLI between the Zn-metal anode and aqueous electrolyte, gelatin, a biodegradable and scalable polypeptide derived from the partial hydrolysis of collagen [44,45], swells and dissolves into 1.25 M ZnSO₄ solution as shown in Figure 1a. Note that, if slightly increased the concentration of ZnSO₄ solution to 1.5 M, the gelatin cannot be completely dissolved into the solution with delamination occurs (Figure S2). Therefore, to maximize the Zn $^{2+}$ ion conductivity, the gelatin solution with 1.25 M ZnSO₄ is chosen to construct the interphase by casting on the bare Zn foil. As illustrated in Figure S3, there are a lot of amino and carboxyl groups in the molecule of gelatin [42]. During the casting process, the gelatin solution gets cured by undergoing a sol–gel process. Meanwhile, the hydroxyl groups present on the Zn foil react with the active carboxyl groups, leading to tight attachment [46]. During the gelation process, the gelatin molecules undergo a conformational change from a

random coil to a triple helix, and non-specific bonds (including hydrogen, electrostatic and hydrophobic bonds) are favored between large chains [42,47].

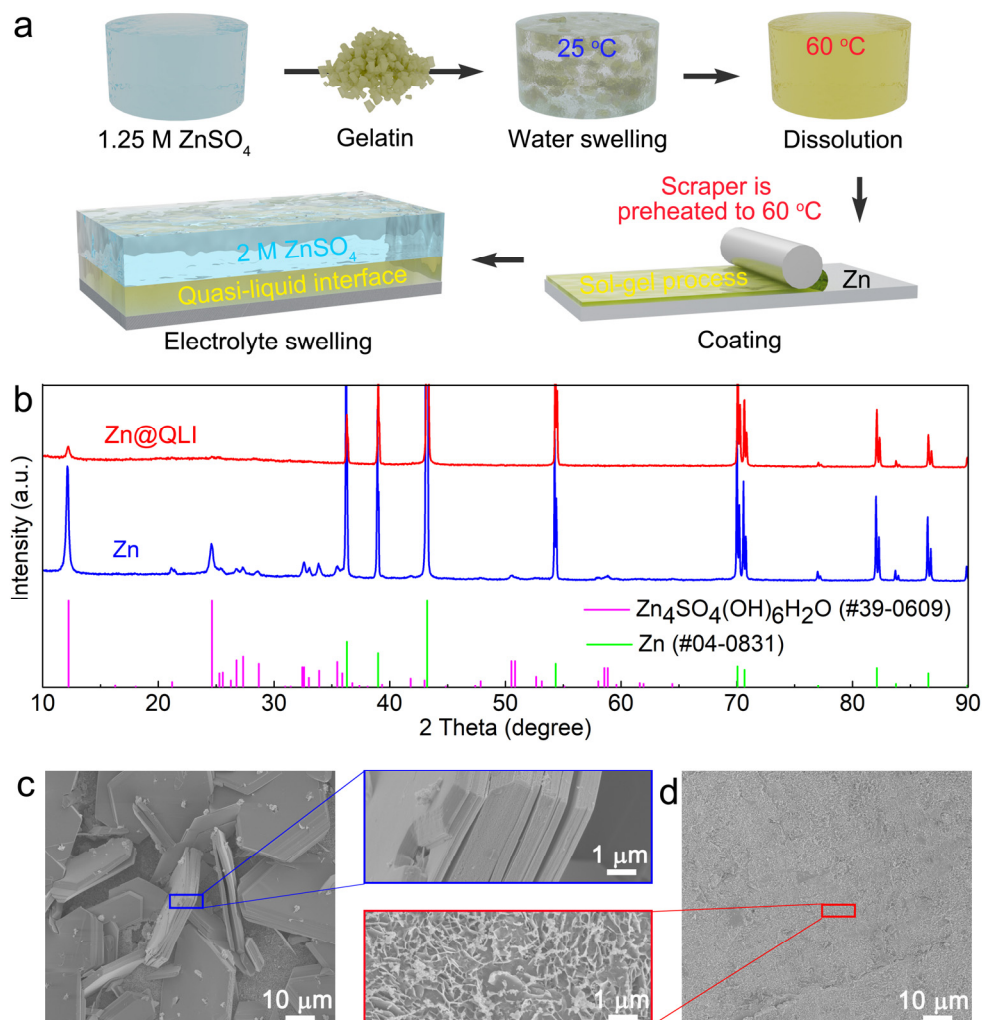


Figure 1. (a) Schematic illustration for the preparation process of Zn@QLI. (b) XRD patterns of Zn and Zn@QLI after immersing in 2 M ZnSO_4 electrolyte for 16 days. SEM images after immersing Zn (c) and Zn@QLI (d) into 2 M ZnSO_4 electrolyte for 16 days.

The interphase displays a certain strength and hardness before immersing into an aqueous electrolyte, as shown in Figure S2b. Benefiting from the gelatin's capability of absorbing 5–10 times its mass in water without losing the cross-linking structure, [42] the interphase swells and becomes transparent without dissolving when immersed into 2 M ZnSO_4 electrolyte (Figure S2c). The insolubility ensures that QLI exists stably instead of dissolving into the electrolyte after being assembled into a cell. Meanwhile, a quasi-liquid characteristic is imparted by the dynamic cross-linking of molecules, enabling QLI to adapt to the surface changes of the Zn anode.

In some previous studies, solid electrolytes constructed with gelatin were used for ZIBs [38,48]. However, in our experiment, the solid gelatin electrolyte melts into a liquid state when the temperature rises to only 40 °C (Figure S4a), which makes the solid-state battery extremely prone to failure during service. By contrast, as the color changes from transparent light yellow to opaque white, the QLI immersed in 2 M ZnSO_4 electrolyte remains in a solid state at 40 °C (Figure S4b). Even if the temperature rises to 60 °C, the QLI still does not dissolve into the electrolyte despite melting into a liquid state (Figure S4c).

The hydrogen-evolution corrosion of the Zn-metal anode in the weakly acidic electrolyte not only destroys the cycle stability of ZMBs but also has a serious impact on its calendar aging. To investigate the corrosion resistance of the anode to the electrolyte, the bare Zn and Zn@QLI pieces were immersed in a 2 M ZnSO₄ electrolyte. The XRD pattern of Zn after soaking for 16 days is shown in Figure 1b. In addition to the Zn phase (PDF#04-0831), a sharp peak exists at around 12.2° (2 Theta) with many miscellaneous peaks, corresponding to the Zn₄SO₄(OH)₆H₂O phase (PDF#39-0609), which demonstrates the occurrence of severe side reactions. By contrast, the XRD pattern of Zn@QLI after immersing shows a smaller main peak without other miscellaneous peaks which corresponds to Zn₄SO₄(OH)₆H₂O phase, suggesting excellent corrosion resistance by introducing the QLI. After 8 days of immersion in 2 M ZnSO₄ electrolyte, as shown in Figure S5a, the surface of Zn becomes rough with nanosheets and micro-sized bulks that are perpendicular and parallel to the surface, respectively. Compared with the nanosheets, the bulks contain less element Zn and more element O, corresponding to the side-reaction product. In comparison, the surface of Zn@QLI is still flat with a few wrinkles, and the distribution of elements Zn and O is uniform on the surface (Figure S5b). After 16 days of immersion, the surface of Zn is further rough and almost completely covered by the large bulks that are oblique to the surface (Figure 1c). In contrast, although the degree of wrinkles is greater, Zn@QLI is still flat (Figure 1d). The composition distribution after immersing for 16 days is not much different from those for 8 days (Figure S6). Clearly, the QLI stably exists on the Zn surface during the calendar process and effectively inhibits the corrosion from the electrolyte.

For aqueous ZMBs, the electrochemical corrosion of electrolytes on the Zn-metal anode is regarded as a significant failure mechanism. The effect of the QLI on corrosion resistance was analyzed by Tafel polarization experiments in 2 M ZnSO₄ electrolyte with a sweep rate of 0.5 mV s⁻¹ (Figure 2a). Compared to the bare Zn anode, the corrosion current density of the Zn@QLI anode decreases by 199 μA cm⁻², indicating a lower corrosion rate. This demonstrates that the QLI effectively prevents the electrolyte from attacking the Zn anode unscrupulously. Different from some previous reports about constructing SEI-like film [49,50], the overpotential of the Zn@QLI anode decreases from −1.016 V of the Zn anode to −1.023 V. This could be caused by the good adhesion of the QLI to the substrate with carboxyl groups, which affects the space charge region of the interface and thus tailors the electrochemical properties of the Zn anode [51].

To further explore the nucleation process and surface change, chronoamperometry (CA) was conducted (Figure 2b). When applying an overpotential of −150 mV, the current density of the Zn anode continually increases within 300 s, suggesting that the Zn²⁺ ion undergoes a 2D diffusion process [52], where Zn²⁺ migrated to the anode surface diffuses laterally along the surface and finds the most energetically favorable sites for charge transfer, leading to many protrusions during the nucleation stage. After the CA test, the surface of the Zn anode is rough with many irregular flaky structures and holes (Figure 2c). The elements Zn and O distribute in these flaky structures evenly (Figure S7a), indicating that the Zn dendrites are formed instead of the side-reaction products. For the Zn@QLI anode, a 2D diffusion occurs within 20 s, and then a stable 3D diffusion continuously proceeds beyond 300 s with a current density of 16.6 mA cm⁻², indicating that the absorbed Zn²⁺ tends to be locally reduced and deposit in very close proximity due to the 2D diffusion barrier of the Gel layer. After the CA test, the Zn@QLI anode still possesses a flat surface without component segregation (Figures 2d and S7b).

The electrochemical stability of the Zn@QLI anode was evaluated by galvanostatic cycling in a symmetric cell with a glass fiber separator. The total capacity corresponding to 20 μm Zn foil is ~11 mAh cm⁻² (Figure S8). As shown in Figure 3a, after cycling for 280 h with a capacity of 1 mAh cm⁻² at 1 mA cm⁻², the voltage of the cell with Zn electrodes displays large fluctuations, and a short circuit occurs. By contrast, the cell with Zn@QLI electrodes exhibits a stable polarization voltage (~70 mV) over 800 h. With decreasing the current density to 0.2 mA cm⁻², the short circuit time for Zn electrodes (330 h) is not much

different from that at 1 mA cm^{-2} (Figure 3b). However, the Zn@QLI electrodes can maintain a stable plating/stripping process over 2500 h with stable polarization voltage (dropping from the initial ~ 30 to $\sim 18 \text{ mV}$ at the end), endowing almost an order improvement in cycling life. The changeless voltage polarization after 700 h demonstrates uniform Zn metal deposition enabled by the QLI. It should be pointed out that the nucleation overpotentials of Zn@QLI are higher than Zn (as shown in Figure S9, 51.0 and 69.9 mV at 1 mA cm^{-2} for Zn@QLI and Zn, and 34.0 and 42.9 mV at 0.2 mA cm^{-2} for Zn@QLI and Zn, respectively). Meanwhile, after the initial cycles, the polarization voltage of Zn@QLI is higher compared with Zn (see inset of Figure 3a,b). The cell with Zn@QLI electrodes can still cycle stably for more than 700 h even increasing the capacity to 3 mAh cm^{-2} at 1 mA cm^{-2} (Figure S10).

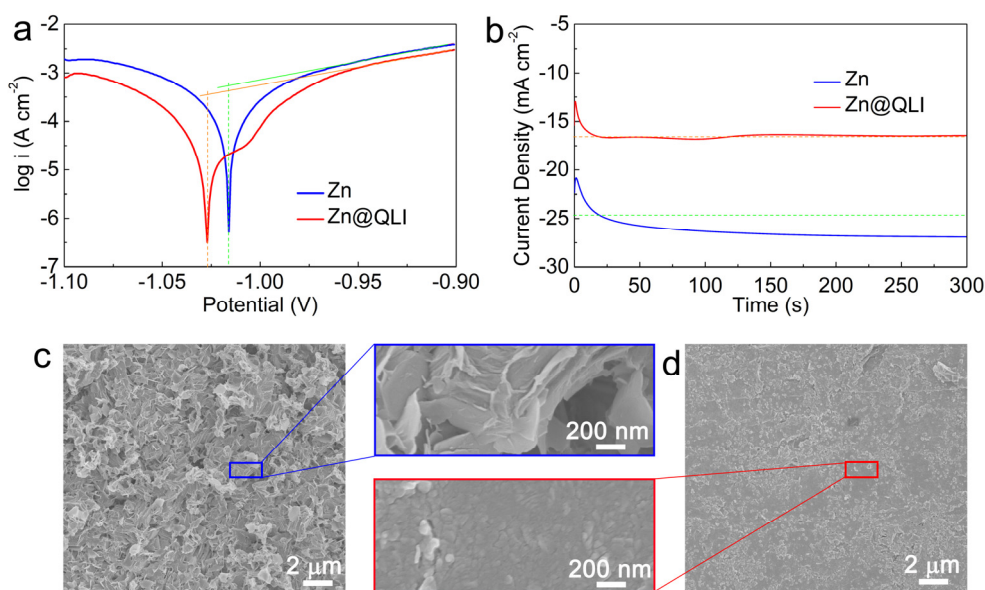


Figure 2. (a) Tafel polarization curves of Zn and Zn@QLI. The green and orange lines indicate corrosion potentials and corrosion currents for Zn and Zn@QLI, respectively. (b) CA curves of Zn and Zn@QLI at a -150 mV overpotential. SEM images of Zn (c) and Zn@QLI (d) after the CA test.

Electrochemical impedance spectroscopies (EIS) of the symmetric cells were tested to explore the origin of the different overpotentials, as shown in Figure 3c. The initial EIS spectra of the cell with Zn electrodes display a depressed semicircle in the tested frequency range (corresponding to the charge transfer resistance (R_{ct})), whereas the spectra with Zn@QLI electrodes exhibit two characteristic semicircles in the high- and middle-frequency range, which corresponds to the R_{ct} and the film resistance (R_f), respectively. The R_f limits the initial diffusion of Zn^{2+} ions on Zn@QLI. As a consequence, the Zn@QLI electrode exhibits larger nucleation overpotential and polarization voltage than the Zn electrode. It is exactly the reason why Zn^{2+} cannot diffuse freely along the lateral surface as revealed by CA (Figure 2b). After cycling for 100 h, the semicircles corresponding to R_f and R_{ct} in the EIS spectra with Zn@QLI electrodes greatly reduce and remain almost unchanged after 300 h cycles, demonstrating that the QLI achieves good compatibility with electrode and electrolyte and remains stable during the subsequent charge/discharge processes.

To explore the essence of cycling stability, the surface morphology of the electrodes after the plating/stripping processes was observed. After only 100 h cycles, the as-deposited bare Zn electrode consists of many nanosheet-like dendrites (Figure 3d). The morphology of the Zn electrode is worse in the stripped state (Figure S11a). By contrast, as shown in the as-deposited and as-stripped Zn@QLI after cycles (Figures 3e and S11b), the quasi-liquid nature enables the QLI to form a fiber-reinforced structure with the glass fiber separator during cycling, benefiting from the long-term stability. This composite structure is hard to be completely removed due to the close integration with the substrate and thus

unable to get a glimpse of the Zn@QLI topography. According to the voltage-time curves (Figure 3a,b), it is reasonable to expect that the QLI effectively inhibits side reactions, as well as zinc dendrites. Compared with the bare Zn electrode, the QLI provides at least three ways to achieve long-cycle stability: (i) suppressing the corrosion and side reactions by eliminating the direct contact between electrolyte and electrode; (ii) inducing smooth surface morphology by changing the diffusion mode of Zn^{2+} ions in the process of zinc nucleation and growth; and (iii) the quasi-liquid characteristic makes the QLI enduringly cover the zinc surface in a conformal manner, which is conducive to the long-term effect of the above two aspects.

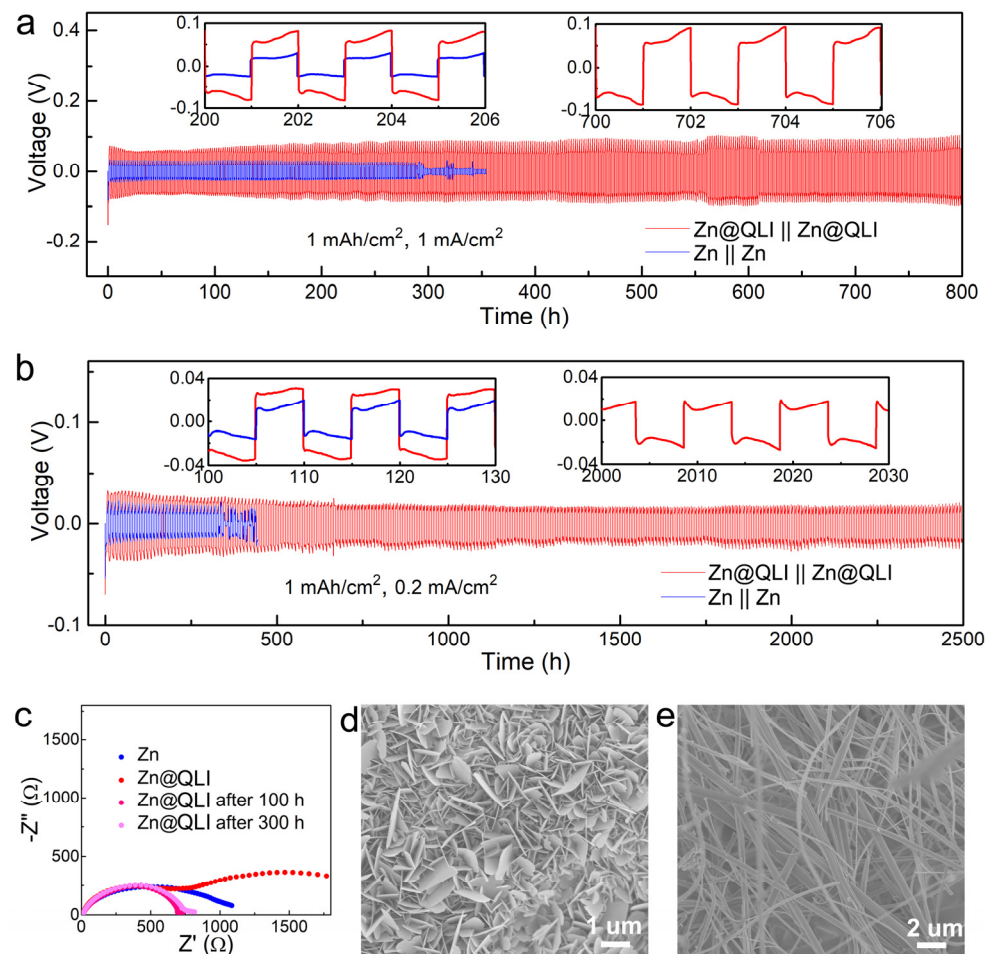


Figure 3. Long-term galvanostatic cycling of symmetric cells with Zn and Zn@QLI electrodes, with a capacity of 1 mAh cm^{-2} at 1 mA cm^{-2} (a) and 0.2 mA cm^{-2} (b). (c) Nyquist plots of Zn and Zn@QLI before and after cycling. SEM images of the Zn (d) and Zn@QLI electrode (e) in the deposited state, after cycling for 100 h with a capacity of 1 mAh cm^{-2} at 0.2 mA cm^{-2} .

To explore the deposition morphology of Zn@QLI under the glass fiber and eliminate the influence of external pressure, a symmetric cell without separators was used (cell configurations, Figure S12), where two electrodes are separated by a polytetrafluoroethylene (PTFE) ring. Post-mortem electrode analyses are conducted to clarify its stability after the plating/stripping processes. After cycling for 30 h, the QLI can be peeled off from Zn@QLI after freeze-drying, and the zinc surface under QLI is smooth (Figure 4a). In contrast, the Zn electrode becomes rough with particles visible to the naked eyes. As immersed in the electrolyte, the XRD pattern of the Zn electrode after cycling for 30 h shown in Figure 4b indicates that the side-reaction products are also dominated by $\text{Zn}_4\text{SO}_4(\text{OH})_6\text{H}_2\text{O}$ phase (the strongest peak at 12.2°). In addition, a clear peak at around 24.6° confirms the pres-

ence of the $\text{ZnSO}_4 \cdot 6\text{H}_2\text{O}$ phase (PDF#32-1478), which should be caused by the pores and pits that make it difficult to wash. In contrast, the Zn@QLI electrode shows a much less $\text{Zn}_4\text{SO}_4(\text{OH})_6\text{H}_2\text{O}$ phase without the presence of $\text{ZnSO}_4 \cdot 6\text{H}_2\text{O}$ phase, demonstrating highly reversible plating/stripping processes and thus excellent interface stability. The different surface states of the electrodes after cycling are further determined by XPS (see Figures S13 and S14 for details).

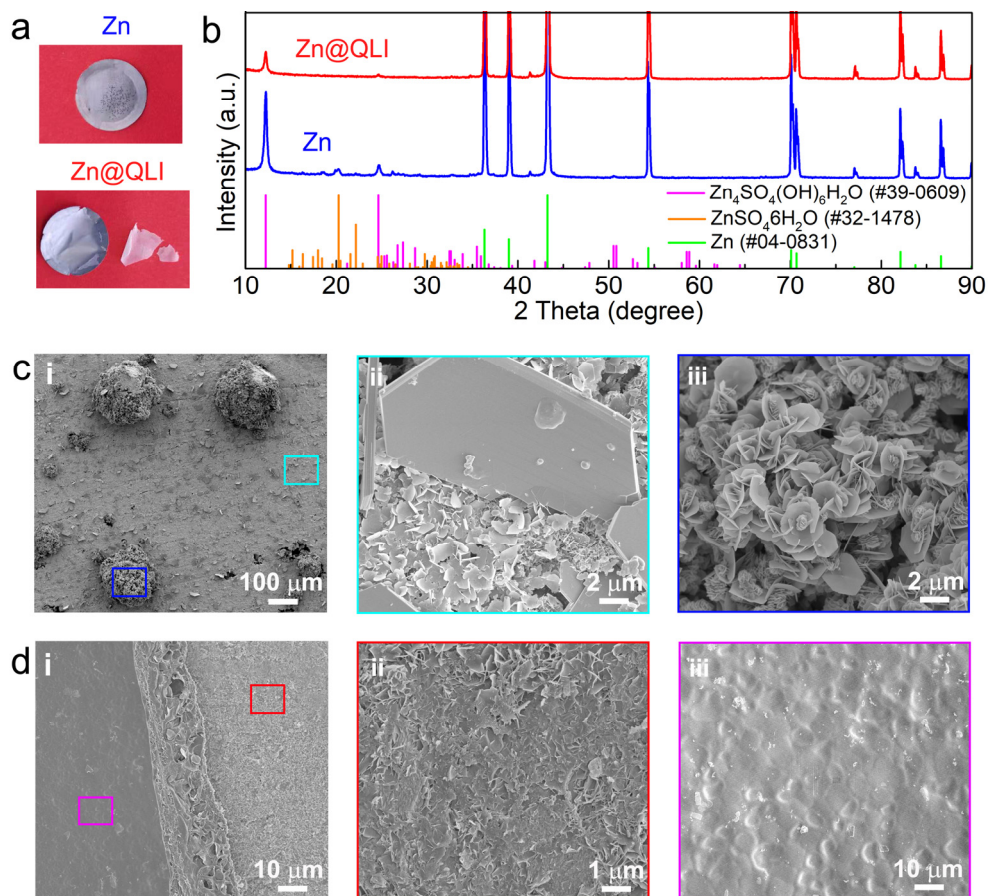


Figure 4. Post-mortem electrode analyses after 30 h cycles with a capacity of 1 mAh cm^{-2} at 0.2 mA cm^{-2} using the symmetric cells without separators. Photos (a) and XRD patterns (b) of Zn and Zn@QLI after cycles. SEM images of Zn (c) and Zn@QLI electrode (d) after cycles in the cross-section view.

As indicated in Figure 4c, these big particles are composed of nano-flowers with evenly distributed elements Zn and O at a ratio of 1.43 (Figure S15a). The relatively flat area actually contains lots of nano-platelets and large bulks of oxygen-contained zinc compounds (Figure S15b). Moreover, as shown in the cross-sectional view (Figure S17a), the big particles are rooted in the base, and the surface of the Zn electrode is loose with deep pits appearing. Figure 4d_i displays the edge of QLI (confirmed by EDS, Figure S16a), showing a tightly bound to the substrate even after freeze-drying. The surface of QLI is smooth (Figure 4d_{iii}) with evenly distributed element C and a small amount of elements Zn and S (derived from zinc sulfate, Figure S16b). Although the zinc surface under QLI becomes rough to a certain extent (Figure 4d_{ii}), it is still much smoother compared to the Zn electrode, with uniform distribution of elements Zn and O (Figure S16c). The cross-section of the Zn@QLI electrode is dense without pores and pits (Figure S17b). In short, the uneven deposition of the bare Zn electrode will be accelerated when external pressure disappears. In comparison, the QLI still maintains a tight bond with the substrate and induces uniform zinc deposition, even if without external pressure.

In the above test of the symmetric cell without separators, the QLI is still fixed under the PTFE ring. To further clarify whether the QLI can still tightly adhere to the zinc foil and induce uniform deposition of zinc metal in a completely free state, a symmetric cell with suspended electrodes immersed in the sufficient electrolyte was used (cell configuration, Figure S18). The results indicate that, even in a state of complete freedom, the QLI still can tightly adhere to the substrate on charge/discharge processes and thus eliminating the direct contact between electrolyte and electrode, as well as regulating the deposition of zinc metal (see Figures S19 and S20 for details).

Furthermore, the zinc deposition on the bare and modified anodes with various classes of coatings was simulated in COMSOL (cell geometry, Figures S21 and S22). For the bare Zn anodes, a large dendrite grows due to the 2D diffusion of Zn^{2+} , causing a region of enhanced Zn^{2+} flux at the top of the Zn dendrite (Figure 5a and Video S1). In contrast, the dendrite growth of Zn@QLI is effectively suppressed with small protrusion appearing, benefiting from the 3D diffusion of the Zn^{2+} ion (Figure 5f). The dynamic behavior enables the QLI to adapt anode change and invariably adhere to its surface with uniform volume changes (Figure 5g). For comparison, the simulations on Zn anode coated with solid-state interphase (SSI, elastic or rigid) are conducted. Small but still obvious Zn dendrite with a hotspot of Zn^{2+} flux appears on the Zn@elastic-SSI with electrolyte filling in the oval gap (Figure 5c), and a high amount of volume change occurs near the root of Zn dendrite (Figure 5d and Video S2). If the oval gap below the elastic SSI is filled with air instead of electrolyte, since the lack of Zn^{2+} ionic conductivity, the phenomena of necking and digging near the root of the Zn dendrite are more significant (Figure S22b,c). For the rigid SSI, a dendrite similar to that on the bare Zn anode appears, but with a greater aspect ratio and concentrated volume change near the dendrite root (Figure S22e,f).

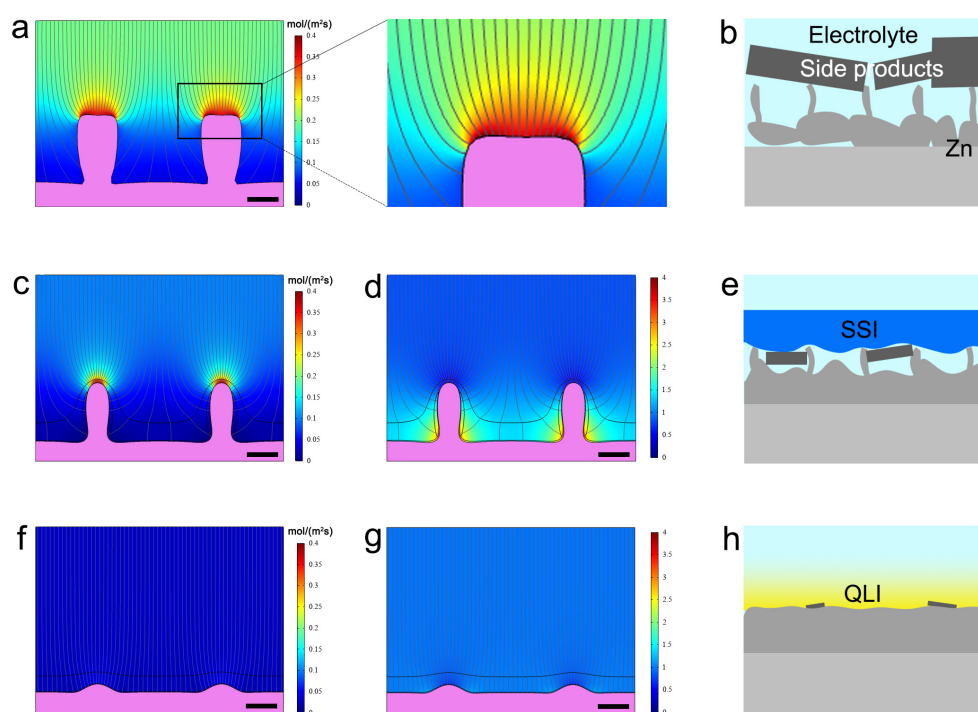


Figure 5. Simulations of Zn deposition on the bare Zn anode (a), Zn@elastic-SSI with electrolyte filling in the oval gap (c) and Zn@QLI (f). The color indicates the magnitude of spatial Zn^{2+} flux. Mesh element volume change during Zn depositing on Zn@SSI with electrolyte filling in the oval gap (d) and Zn@QLI (g). The color indicates the degree of volume change. In each snapshot, the streamlines display the direction of Zn^{2+} flux and the electrode is painted pink. Scale bar: 10 μ m. Schematic illustrating the Zn plating/stripping behaviors for the bare Zn anode (b), Zn@SSI (e) and Zn@QLI (h).

In terms of the experiment and simulation results above, the deposition behavior of Zn on the bare anode and the modified anode is illustrated in the right panel of Figure 5. For the bare Zn anode, side reactions and dendrites occur without restraint, causing low CE and a short lifetime. (Figure 5b). For the Zn@SSI (including elastic and rigid) anode, suppressed but still inevitable dendrites and side reactions occur, since the SSI cannot enduringly cling to the electrode closely during cycling (Figure 5e). By comparison, the dynamic behavior of QLI ensures the uniform transportation of Zn^{2+} on the anode over the entire cycle life, thus avoiding the unscrupulous growth of dendrites and side reactions (Figure 5h).

To examine the reversibility of the modified anode in an aqueous electrolyte, a plating/stripping test was conducted in the half cells with Cu or Cu@QLI as the current collector and bare Zn as an anode. Figure 6a shows their CEs with a capacity of 1 mAh cm^{-2} at 1 mA cm^{-2} , and corresponding voltage profiles are shown in Figure S23. After 100 cycles, the Cu-Zn half cell fails with a fluctuant voltage file, while the Cu@QLI-Zn half cell cycles stably more than 220 cycles with a CE of 99.5%. In addition, by reducing the current density to 0.2 mA cm^{-2} or increasing the capacity to 3 mAh cm^{-2} (as shown in Figure S24), which is thought to exacerbate the irreversible reactions of the Zn-metal anode, the CEs of the Cu@QLI are superior to the bare Cu.

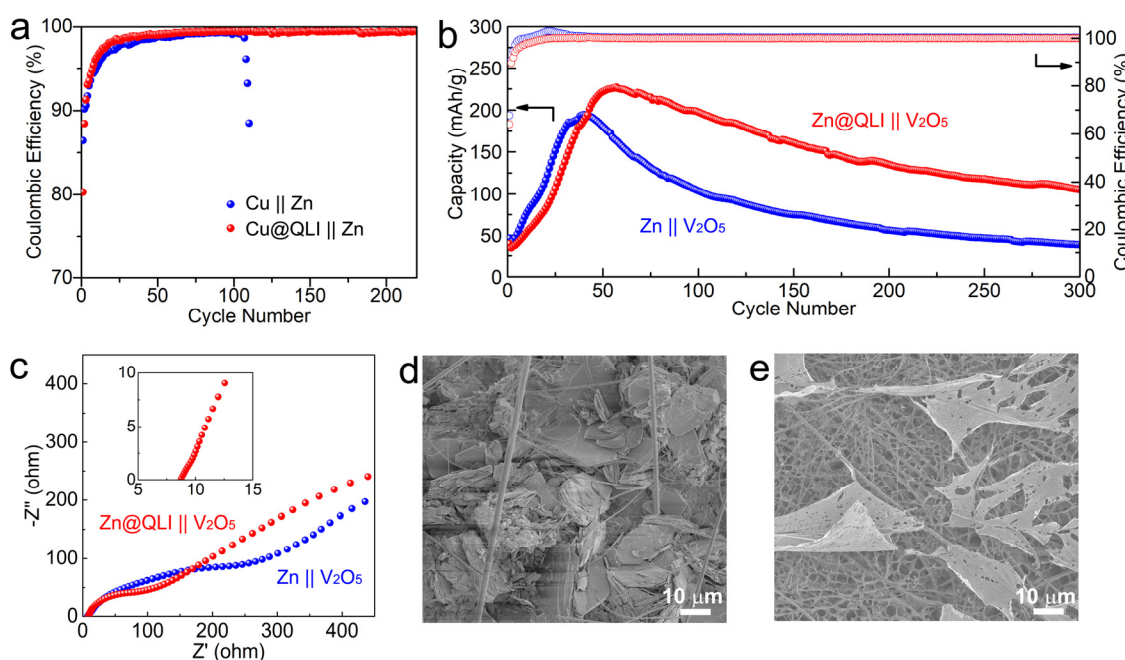


Figure 6. (a) Coulombic efficiency of the half cells with a capacity of 1 mAh cm^{-2} at 1 mA cm^{-2} . (b) Cycling performance of the full cells within $0.2\text{--}1.6 \text{ V}$ at 365 mAh g^{-1} . (c) Nyquist plots of the full cells after 300 cycles. SEM images of the Zn (d) and Zn@QLI anode (e) after 300 cycles.

To explore the potential of practical applications, full prototype coin-type cells were assembled with the V_2O_5 as a cathode and the Zn or Zn@QLI as an anode. After the initial ~50 cycles of activation, the specific capacity of the Zn@QLI- V_2O_5 full cell reaches 226.6 mAh g^{-1} , as shown in Figure 6b, and remains 105.3 mAh g^{-1} after 300 cycles with a Coulombic efficiency (CE) of almost 100%. However, the specific capacity of the Zn- V_2O_5 full cell reaches 194.5 mAh g^{-1} after initial activation, and only a specific capacity of 38.5 mAh g^{-1} remains after 300 cycles. The galvanostatic charge/discharge curves and cyclic voltammetry (CV) profiles of the two cells present a similar two-step redox process and potential with high reversibility (Figure S25). The improved electrochemical stability of the full cells is analyzed by testing EIS after 300 cycles, where Zn- V_2O_5 and Zn@QLI- V_2O_5 cells exhibit two semicircles in the high- and middle-frequency range, corresponding to R_{ct}

and R_f , respectively (Figure 6c). Compared to the Zn@QLI-V₂O₅ full cell, Zn-V₂O₅ displays a much larger R_f and R_{ct} , originating from the rough surface with lots of large bulks of zinc oxides as revealed by the post-mortem morphology and element analyses of the anode surface (Figures 6d and S26a). In contrast, as demonstrated in the symmetric cell above, a smooth glass-fiber-reinforced structure is formed on the QLI during cycling (Figures 6e and S26b), which stabilizes the interphase and ensures long-term electrochemical stability. The self-discharge rate of the Zn@QLI-V₂O₅ full cell is 7.1%, evaluated by standing for 3 days after being fully charged (Figure S27).

4. Conclusions

In summary, a QLI with a “solid–liquid” property is constructed on the Zn-metal anode in an aqueous electrolyte. The solid characteristic of QLI ensures its stable existence between the anode and electrolyte, and the liquid behavior imparted by electrolyte swelling and cross-linking of gelatin molecules enables the interphase dynamic and self-adaptive to the anode evolution. Consequently, by enduringly inhibiting the unscrupulous attack from the electrolyte and free diffusion of Zn²⁺, the Zn@QLI anode remains dendrite-free and significantly reduces side reactions during either aging or plating/stripping processes. A glass-fiber-reinforced QLI is formed during cycling, enabling the symmetric cell with Zn@QLI electrode to deliver long-time cycling with a 10-fold enhancement compared to the bare Zn. Meanwhile, the half and full cells modified with QLI display a superior CE and capacity retention than that without modification, respectively. The results demonstrate the significance of tight coupling between the modified layer and the anode, not only in the aging period but also in the repeated charge/discharge processes of the cell.

Supplementary Materials: The following supporting information can be downloaded at <https://www.mdpi.com/article/10.3390/batteries9060328/s1> [42,53,54], Figures S1–S27: material characterizations and electrochemical tests; Video S1: simulations of zinc deposition; Video S2: volume changes of mesh element.

Author Contributions: Conceptualization, methodology, investigation, data curation and writing—original draft preparation, J.W. (Junzhang Wang); formal analysis, Z.X., T.Q., J.W. (Jintian Wang) and R.T.; conceptualization, supervision, funding acquisition and writing—review and editing, X.G.; software, Z.W.; supervision, Z.L. and H.Y. All authors have read and agreed to the published version of the manuscript.

Funding: This work is supported by the National Natural Science Foundation of China (21875217 and 51372225).

Data Availability Statement: The data that support the findings of this study are available from the corresponding author upon reasonable request.

Conflicts of Interest: The authors declare no conflict of interest.

References

- Wang, R.; Li, H.; Wu, Y.; Li, H.; Zhong, B.; Sun, Y.; Wu, Z.; Guo, X. How to Promote the Industrial Application of SiO_x Anode Prelithiation: Capability, Accuracy, Stability, Uniformity, Cost, and Safety. *Adv. Energy Mater.* **2022**, *12*, 2202342. [[CrossRef](#)]
- Wu, D.; Wu, F. Toward better batteries: Solid-state battery roadmap 2035+. *eTransportation* **2023**, *16*, 100224. [[CrossRef](#)]
- Wei, Z.; Zhang, N.; Feng, T.; Wu, F.; Zhao, T.; Chen, R. A copolymer microspheres-coated separator to enhance thermal stability of lithium-sulfur batteries. *Chem. Eng. J.* **2022**, *430*, 132678. [[CrossRef](#)]
- Yun, F.; Liu, S.; Gao, M.; Bi, X.; Zhao, W.; Chang, Z.; Yuan, M.; Li, J.; Shen, X.; Qi, X.; et al. Investigation on step overcharge to self-heating behavior and mechanism analysis of lithium ion batteries. *J. Energy Chem.* **2023**, *79*, 301–311. [[CrossRef](#)]
- Zhang, J.G.; Xu, W.; Xiao, J.; Cao, X.; Liu, J. Lithium Metal Anodes with Nonaqueous Electrolytes. *Chem. Rev.* **2020**, *120*, 13312–13348. [[CrossRef](#)] [[PubMed](#)]
- Liu, D.-H.; Bai, Z.; Li, M.; Yu, A.; Luo, D.; Liu, W.; Yang, L.; Lu, J.; Amine, K.; Chen, Z. Developing high safety Li-metal anodes for future high-energy Li-metal batteries: Strategies and perspectives. *Chem. Soc. Rev.* **2020**, *49*, 5407–5445. [[CrossRef](#)]
- Han, C.; Li, W.; Liu, H.K.; Dou, S.; Wang, J. Principles and strategies for constructing a highly reversible zinc metal anode in aqueous batteries. *Nano Energy* **2020**, *74*, 104880. [[CrossRef](#)]
- Yang, C.; Xia, J.; Cui, C.; Pollard, T.P.; Vatamanu, J.; Faraone, A.; Dura, J.A.; Tyagi, M.; Kattan, A.; Thimsen, E. All-temperature zinc batteries with high-entropy aqueous electrolyte. *Nat. Sustain.* **2023**, *6*, 1–11. [[CrossRef](#)]

9. Lu, X.; Yang, P.; Xu, H.; Xiao, L.; Liu, L.; Li, R.; Alekseeva, E.; Zhang, J.; Levin, O.; An, M. Biomass derived robust Fe4N active sites supported on porous carbons as oxygen reduction reaction catalysts for durable Zn-air batteries. *J. Mater. Chem. A* **2023**, *11*, 3725–3734. [[CrossRef](#)]
10. Karbak, M.; Baazizi, M.; Sayah, S.; Autret-Lambert, C.; Tison, Y.; Martinez, H.; Chafik, T.; Ghamouss, F. Unraveling high-performance oxygen-deficient amorphous manganese oxide as the cathode for advanced zinc ion batteries. *J. Mater. Chem. A* **2023**, *11*, 2634–2640. [[CrossRef](#)]
11. Han, J.; Euchner, H.; Kuenzel, M.; Hosseini, S.M.; Groß, A.; Varzi, A.; Passerini, S. A Thin and Uniform Fluoride-Based Artificial Interphase for the Zinc Metal Anode Enabling Reversible Zn/MnO₂ Batteries. *ACS Energy Lett.* **2021**, *6*, 3063–3071. [[CrossRef](#)]
12. Cao, L.; Li, D.; Pollard, T.; Deng, T.; Zhang, B.; Yang, C.; Chen, L.; Vatamanu, J.; Hu, E.; Hourwitz, M.J. Fluorinated interphase enables reversible aqueous zinc battery chemistries. *Nat. Nanotechnol.* **2021**, *16*, 1–9. [[CrossRef](#)] [[PubMed](#)]
13. Zhang, J.; Dou, Q.; Yang, C.; Zang, L.; Yan, X. Polyiodide shuttle inhibition in ethylene glycol-added aqueous electrolytes for high energy and long-term cyclability of zinc-iodine batteries. *J. Mater. Chem. A* **2023**, *11*, 3632–3639. [[CrossRef](#)]
14. Li, Z.; Wu, L.; Dong, S.; Xu, T.; Li, S.; An, Y.; Jiang, J.; Zhang, X. Pencil Drawing Stable Interface for Reversible and Durable Aqueous Zinc-Ion Batteries. *Adv. Funct. Mater.* **2020**, *31*, 2006495. [[CrossRef](#)]
15. Zhou, S.; Wang, Y.; Lu, H.; Zhang, Y.; Fu, C.; Usman, I.; Liu, Z.; Feng, M.; Fang, G.; Cao, X.; et al. Anti-Corrosive and Zn-Ion-Regulating Composite Interlayer Enabling Long-Life Zn Metal Anodes. *Adv. Funct. Mater.* **2021**, *10*, 2104361. [[CrossRef](#)]
16. Chuai, M.; Yang, J.; Wang, M.; Yuan, Y.; Liu, Z.; Xu, Y.; Yin, Y.; Sun, J.; Zheng, X.; Chen, N.; et al. High-performance Zn battery with transition metal ions co-regulated electrolytic MnO₂. *eScience* **2021**, *1*, 178–185. [[CrossRef](#)]
17. Zhang, X.T.; Li, J.X.; Liu, D.Y.; Liu, M.K.; Zhou, T.S.; Qi, K.W.; Shi, L.; Zhu, Y.C.; Qian, Y.T. Ultra-long-life and highly reversible Zn metal anodes enabled by a desolvation and deionization interface layer dagger. *Energy Environ. Sci.* **2021**, *14*, 3120–3129. [[CrossRef](#)]
18. Leng, K.; Li, G.; Guo, J.; Zhang, X.; Wang, A.; Liu, X.; Luo, J. A Safe Polyzwitterionic Hydrogel Electrolyte for Long-Life Quasi-Solid State Zinc Metal Batteries. *Adv. Funct. Mater.* **2020**, *30*, 2001317. [[CrossRef](#)]
19. Xu, L.; Meng, T.; Zheng, X.; Li, T.; Brozena, A.H.; Mao, Y.; Zhang, Q.; Clifford, B.C.; Rao, J.; Hu, L. Nanocellulose-Carboxymethylcellulose Electrolyte for Stable, High-Rate Zinc-Ion Batteries. *Adv. Funct. Mater.* **2023**, *2302098*. [[CrossRef](#)]
20. Wu, M.; Zhang, Y.; Xu, L.; Yang, C.; Hong, M.; Cui, M.; Clifford, B.C.; He, S.; Jing, S.; Yao, Y.; et al. A sustainable chitosan-zinc electrolyte for high-rate zinc-metal batteries. *Matter* **2022**, *5*, 3402–3416. [[CrossRef](#)]
21. Li, M.; Wang, X.; Hu, J.; Zhu, J.; Niu, C.; Zhang, H.; Li, C.; Wu, B.; Han, C.; Mai, L. Comprehensive H₂O Molecules Regulation via Deep Eutectic Solvents for Ultra-Stable Zinc Metal Anode. *Angew. Chem. Int. Ed.* **2023**, *62*, 202215552.
22. Wu, C.; Tan, H.T.; Huang, W.J.; Li, W.X.; Dinh, K.N.; Yan, C.S.; Wei, W.F.; Chen, L.B.; Yan, Q.Y. A New Scalable Preparation of Metal Nanosheets: Potential Applications for Aqueous Zn-Ion Batteries Anode. *Adv. Funct. Mater.* **2020**, *30*, 2003187. [[CrossRef](#)]
23. Zhou, J.; Xie, M.; Wu, F.; Mei, Y.; Hao, Y.; Li, L.; Chen, R. Encapsulation of Metallic Zn in a Hybrid MXene/Graphene Aerogel as a Stable Zn Anode for Foldable Zn-Ion Batteries. *Adv. Mater.* **2021**, *34*, 2106897. [[CrossRef](#)] [[PubMed](#)]
24. Cai, Z.; Ou, Y.; Zhang, B.; Wang, J.; Fu, L.; Wan, M.; Li, G.; Wang, W.; Wang, L.; Jiang, J.; et al. A Replacement Reaction Enabled Interdigitated Metal/Solid Electrolyte Architecture for Battery Cycling at 20 mA cm⁻² and 20 mAh cm⁻². *J. Am. Chem. Soc.* **2021**, *143*, 3143–3152. [[CrossRef](#)]
25. Chu, Y.; Zhang, S.; Wu, S.; Hu, Z.; Cui, G.; Luo, J. In situ built interphase with high interface energy and fast kinetics for high performance Zn metal anodes. *Energy Environ. Sci.* **2021**, *14*, 3609–3620. [[CrossRef](#)]
26. Shin, J.; Lee, J.; Kim, Y.; Park, Y.; Kim, M.; Choi, J.W. Highly Reversible, Grain-Directed Zinc Deposition in Aqueous Zinc Ion Batteries. *Adv. Energy Mater.* **2021**, *11*, 2100676. [[CrossRef](#)]
27. Guo, X.; Zhang, Z.; Li, J.; Luo, N.; Chai, G.-L.; Miller, T.S.; Lai, F.; Shearing, P.; Brett, D.J.L.; Han, D.; et al. Alleviation of Dendrite Formation on Zinc Anodes via Electrolyte Additives. *ACS Energy Lett.* **2021**, *6*, 395–403. [[CrossRef](#)]
28. Cao, L.; Li, D.; Hu, E.; Xu, J.; Deng, T.; Ma, L.; Wang, Y.; Yang, X.Q.; Wang, C. Solvation Structure Design for Aqueous Zn Metal Batteries. *J. Am. Chem. Soc.* **2020**, *142*, 21404–21409. [[CrossRef](#)]
29. Zhang, Q.; Ma, Y.; Lu, Y.; Zhou, X.; Lin, L.; Li, L.; Yan, Z.; Zhao, Q.; Zhang, K.; Chen, J. Designing Anion-Type Water-Free Zn²⁺ Solvation Structure for Robust Zn Metal Anode. *Angew. Chem.* **2021**, *60*, 23357–23364. [[CrossRef](#)]
30. Hu, K.; Guan, X.; Lv, R.; Li, G.; Hu, Z.; Ren, L.; Wang, A.; Liu, X.; Luo, J. Stabilizing zinc metal anodes by artificial solid electrolyte interphase through a surface ion-exchanging strategy. *Chem. Eng. J.* **2020**, *396*, 125363. [[CrossRef](#)]
31. Liu, X.; Yang, F.; Xu, W.; Zeng, Y.; He, J.; Lu, X. Zeolitic Imidazolate Frameworks as Zn(2+) Modulation Layers to Enable Dendrite-Free Zn Anodes. *Adv. Sci. (Weinh.)* **2020**, *7*, 2002173. [[CrossRef](#)]
32. Ma, L.; Li, Q.; Ying, Y.; Ma, F.; Chen, S.; Li, Y.; Huang, H.; Zhi, C. Toward Practical High-Areal-Capacity Aqueous Zinc-Metal Batteries: Quantifying Hydrogen Evolution and a Solid-Ion Conductor for Stable Zinc Anodes. *Adv. Mater.* **2021**, *33*, 2007406. [[CrossRef](#)]
33. Xie, X.; Liang, S.; Gao, J.; Guo, S.; Guo, J.; Wang, C.; Xu, G.; Wu, X.; Chen, G.; Zhou, J. Manipulating the ion-transfer kinetics and interface stability for high-performance zinc metal anodes. *Energy Environ. Sci.* **2020**, *13*, 503–510. [[CrossRef](#)]
34. Zhao, R.; Yang, Y.; Liu, G.; Zhu, R.; Huang, J.; Chen, Z.; Gao, Z.; Chen, X.; Qie, L. Redirected Zn Electrodeposition by an Anti-Corrosion Elastic Constraint for Highly Reversible Zn Anodes. *Adv. Funct. Mater.* **2020**, *31*, 2001867. [[CrossRef](#)]
35. Kang, L.; Cui, M.; Jiang, F.; Gao, Y.; Luo, H.; Liu, J.; Liang, W.; Zhi, C. Nanoporous CaCO₃. Coatings Enabled Uniform Zn Stripping/Plating for Long-Life Zinc Rechargeable Aqueous Batteries. *Adv. Energy Mater.* **2018**, *8*, 1801090. [[CrossRef](#)]

36. Liang, P.; Yi, J.; Liu, X.; Wu, K.; Wang, Z.; Cui, J.; Liu, Y.; Wang, Y.; Xia, Y.; Zhang, J. Highly Reversible Zn Anode Enabled by Controllable Formation of Nucleation Sites for Zn-Based Batteries. *Adv. Funct. Mater.* **2020**, *30*, 1908528. [[CrossRef](#)]
37. Yang, H.; Chang, Z.; Qiao, Y.; Deng, H.; Mu, X.; He, P.; Zhou, H. Constructing a super-saturated electrolyte front surface for stable rechargeable aqueous zinc batteries. *Angew. Chem. Int. Ed.* **2020**, *59*, 9377–9381. [[CrossRef](#)] [[PubMed](#)]
38. Han, Q.; Chi, X.; Liu, Y.; Wang, L.; Du, Y.; Ren, Y.; Liu, Y. An inorganic salt reinforced Zn²⁺-conducting solid-state electrolyte for ultra-stable Zn metal batteries. *J. Mater. Chem. A* **2019**, *7*, 22287–22295. [[CrossRef](#)]
39. Tan, L.; Lan, X.; Chen, J.; Zhang, H.; Hu, R.; Zhu, M. LiF-Induced Stable Solid Electrolyte Interphase for a Wide Temperature SnO₂-Based Anode Extensible to –50 °C. *Adv. Energy Mater.* **2021**, *11*, 2101855. [[CrossRef](#)]
40. Wang, Q.; Zhao, C.; Wang, J.; Yao, Z.; Wang, S.; Kumar, S.G.H.; Ganapathy, S.; Eustace, S.; Bai, X.; Li, B.; et al. High entropy liquid electrolytes for lithium batteries. *Nat. Commun.* **2023**, *14*, 440. [[CrossRef](#)]
41. Feng, G.; Jia, H.; Shi, Y.; Yang, X.; Liang, Y.; Engelhard, M.H.; Zhang, Y.; Yang, C.; Xu, K.; Yao, Y.; et al. Imaging solid-electrolyte interphase dynamics using operando reflection interference microscopy. *Nat. Nanotechnol.* **2023**, *2*, 1–10. [[CrossRef](#)] [[PubMed](#)]
42. Wang, X.; Ao, Q.; Tian, X.; Fan, J.; Tong, H.; Hou, W.; Bai, S. Gelatin-Based Hydrogels for Organ 3D Bioprinting. *Polymers* **2017**, *9*, 401. [[CrossRef](#)] [[PubMed](#)]
43. Cong, J.; Shen, X.; Wen, Z.; Wang, X.; Peng, L.; Zeng, J.; Zhao, J. Ultra-stable and highly reversible aqueous zinc metal anodes with high preferred orientation deposition achieved by a polyanionic hydrogel electrolyte. *Energy Storage Mater.* **2020**, *35*, 586–594. [[CrossRef](#)]
44. Liu, D.; Nikoo, M.; Boran, G.; Zhou, P.; Regenstein, J.M. Collagen and gelatin. *Annu. Rev. Food Sci. Technol.* **2015**, *6*, 527–557. [[CrossRef](#)]
45. Rodríguez-Rodríguez, R.; Espinosa-Andrews, H.; Velasquillo-Martínez, C.; García-Carvajal, Z.Y. Composite hydrogels based on gelatin, chitosan and polyvinyl alcohol to biomedical applications: A review. *Int. J. Polym. Mater. Polym. Biomater.* **2019**, *69*, 1–20. [[CrossRef](#)]
46. Wang, J.; Fan, M.; Bian, X.; Yu, M.; Wang, T.; Liu, S.; Yang, Y.; Tian, Y.; Guan, R. Enhanced magnetic heating efficiency and thermal conductivity of magnetic nanofluids with FeZrB amorphous nanoparticles. *J. Magn. Magn. Mater.* **2018**, *465*, 480–488. [[CrossRef](#)]
47. Xing, Q.; Yates, K.; Vogt, C.; Qian, Z.; Frost, M.C.; Zhao, F. Increasing mechanical strength of gelatin hydrogels by divalent metal ion removal. *Sci. Rep.* **2014**, *4*, 4706. [[CrossRef](#)]
48. Han, Q.; Chi, X.; Zhang, S.; Liu, Y.; Zhou, B.; Yang, J.; Liu, Y. Durable, flexible self-standing hydrogel electrolytes enabling high-safety rechargeable solid-state zinc metal batteries. *J. Mater. Chem. A* **2018**, *6*, 23046–23054. [[CrossRef](#)]
49. Cao, Z.; Zhu, X.; Xu, D.; Dong, P.; Chee, M.O.L.; Li, X.; Zhu, K.; Ye, M.; Shen, J. Eliminating Zn dendrites by commercial cyanoacrylate adhesive for zinc ion battery. *Energy Storage Mater.* **2021**, *36*, 132–138. [[CrossRef](#)]
50. Zeng, X.; Xie, K.; Liu, S.; Zhang, S.; Hao, J.; Liu, J.; Pang, W.K.; Liu, J.; Rao, P.; Wang, Q. Bio-inspired design of an in situ multifunctional polymeric solid-electrolyte interphase for Zn metal anode cycling at 30 mA cm^{−2} and 30 mA h cm^{−2}. *Energy Environ. Sci.* **2021**, *14*, 5947–5957. [[CrossRef](#)]
51. Yan, M.; Dong, N.; Zhao, X.; Sun, Y.; Pan, H. Tailoring the Stability and Kinetics of Zn Anodes through Trace Organic Polymer Additives in Dilute Aqueous Electrolyte. *ACS Energy Lett.* **2021**, *6*, 3236–3243. [[CrossRef](#)]
52. Zhao, Z.; Zhao, J.; Hu, Z.; Li, J.; Li, J.; Zhang, Y.; Wang, C.; Cui, G. Long-life and deeply rechargeable aqueous Zn anodes enabled by a multifunctional brightener-inspired interphase. *Energy Environ. Sci.* **2019**, *12*, 1938–1949. [[CrossRef](#)]
53. Chen, C.-H.; Pao, C.-W. Phase-field study of dendritic morphology in lithium metal batteries. *J. Power Sources* **2021**, *484*, 229203. [[CrossRef](#)]
54. Liu, K.; Pei, A.; Lee, H.R.; Kong, B.; Liu, N.; Lin, D.; Liu, Y.; Liu, C.; Hsu, P.C.; Bao, Z.; et al. Lithium Metal Anodes with an Adaptive "Solid-Liquid" Interfacial Protective Layer. *J. Am. Chem. Soc.* **2017**, *139*, 4815–4820. [[CrossRef](#)] [[PubMed](#)]

Disclaimer/Publisher's Note: The statements, opinions and data contained in all publications are solely those of the individual author(s) and contributor(s) and not of MDPI and/or the editor(s). MDPI and/or the editor(s) disclaim responsibility for any injury to people or property resulting from any ideas, methods, instructions or products referred to in the content.